Self-archived version of the article published in Chemical Engineering Science:

N. Cancilla, L. Gurreri, M. Ciofalo, A. Cipollina, A. Tamburini, G. Micale

Hydrodynamics and mass transfer in straight fiber bundles with non-uniform porosity, Chemical Engineering Science, 279, 2023, 118935.

https://doi.org/10.1016/j.ces.2023.118935

Hydrodynamics and mass transfer in straight fiber bundles with non-uniform porosity

N. Cancilla[1], L. Gurreri[2*], M. Ciofalo[1], A. Cipollina[1], A. Tamburini[1], G. Micale[1]

[1]*Dipartimento di Ingegneria, Università degli Studi di Palermo*
Viale delle Scienze Ed. 6, 90128 Palermo, Italy

[2]*Dipartimento di Ingegneria Elettrica, Elettronica e Informatica, Università di Catania*
Viale Andrea Doria 6 Ed. 3, 95125 Catania, Italy

[*]corresponding author: luigi.gurreri@unict.it

Abstract

The present study investigates the effects of non-uniformity of bundle porosity by considering a model channel made up of "dense" (low porosity) and "loose" (high porosity) regions. In a simplified treatment, they are assumed to be non-interacting and the flow and scalar concentration fields to be fully developed, requiring previously obtained results for the Darcy permeability and the Sherwood number. Then, 3-D CFD simulations are conducted for a checkerboard arrangement of alternately "dense" and "loose" regions with square-arrayed fibers, accounting for entry effects and interactions. Non-uniformity causes a significant increase of the permeability and a strong reduction of the Sherwood number. The effects are larger, approaching those obtained for non-interacting regions, if the regions' length scale is large. The attainment of fully developed conditions is greatly shifted forward in non-uniform bundles and the mass transfer development length may largely exceed the physical length of most hollow-fiber devices.

Keywords: Hollow fiber; non-uniform porosity; Darcy permeability; Sherwood number; CFD; entry effects

1. Introduction

The widespread use of hollow fiber membrane contactors in various fields of engineering (e.g. chemical, biomedical, environmental) has led to an ever-increasing interest in the modeling of the phenomena involving fluid dynamics and mass transfer in these systems.

During the last decades, research efforts have focused on the effects on the performances of such features as fiber internal diameter, gas permeance, selectivity (Lemanski and Lipscomb, 2000; Lipscomb and Sonalkar, 2004; Liu et al., 2001); or the influence of the fluid flow distribution both in the lumen (Park and Chang, 1986) and in the shell side (Kim et al., 2013, 2009; Łabęcki et al., 1995; Lemanski and Lipscomb, 2002, 1995; Noda et al., 1979).

The effects of the design of the shell side inlet and outlet ports have also been investigated experimentally (Frank et al., 2001, 2000) and computationally (Ding et al., 2004), as well as the possibility of improving a module's performance by using new geometries, alternative to the commercial ones (Cancilla et al., 2022).

The comparison of fluid dynamics and mass transfer in regular arrays (Cancilla et al., 2021; Happel, 1959; Ishimi et al., 1987; Miyagi, 1958; Noda and Gryte, 1979; Sparrow and Loeffler, 1959) as opposed to random distributions (Wang et al., 2003) of hollow fibers has been investigated for both the constant wall flux condition (Bao and Lipscomb, 2002a) and the constant wall concentration one (Bao and Lipscomb, 2002b), and mass transfer entry effects have also been studied (Bao et al., 1999). A recent paper (Sun et al., 2022) focused on the effects of a non-uniform porosity at the fibers-module case interface on the performance of a gas separation module.

The porosity may be unequally distributed over the cross section of the bundle. Such condition is very common in real hollow fiber bundles used in several membrane contactors, for example due to the manufacturing process or as the result of the interaction of the flow with the fiber bundle (Ando et al. 2022). **Figure 1** shows a sketch of two portions of a bundle, arranged in a regular square and hexagonal lattice, in comparison with photographs of a cross section for a real fiber bundle (hemodialyzer), with details of two portions of different local porosity. The photograph in **Figure 1**(c) shows the simultaneous presence of regions of higher packing density (low porosity) and regions of lower packing density (high porosity). In particular, the observation of **Figure 1**(c) confirms the presence of a wide central region of the photographed bundle portion characterized by a significant void fraction opposed to the neighboring bundle regions characterized by the presence of fibers that almost touch each other.

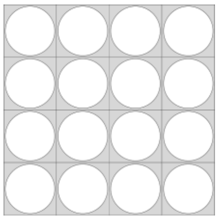

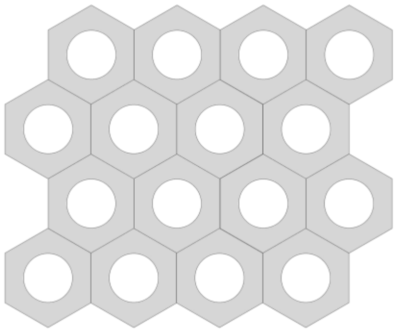

(a) (b)

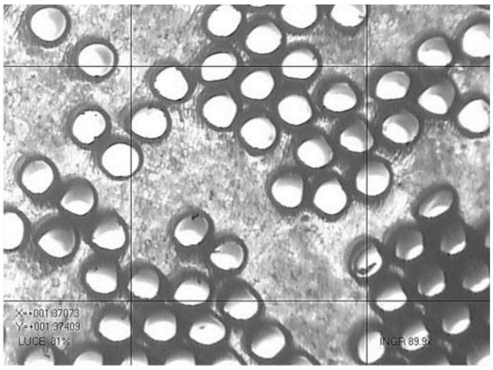

(c)

Figure 1: Top: schematic representation of regular arrays of hollow fibers, arranged in (a) a square lattice and (b) a hexagonal lattice. Bottom: photograph of a real hollow fiber bundle, showing regions of higher packing density (low porosity) and regions of lower packing density (high porosity).

The non-uniformity may vary in amount and in length scale according to the specific application and may affect both hydrodynamics and mass transfer.

Lipscomb and co-workers studied (Bao et al., 1999) these effects on mass transfer in the entry region by solving the governing equations under the boundary layer approximation. They concluded that mass transfer coefficients in random hollow fiber bundles are much lower than in regular arrays.

In subsequent work (Bao and Lipscomb, 2002a, 2002b) the authors extended their investigation to the fully developed region. The results are surprising: the random fiber packing significantly reduces mass transfer coefficients, much more in the well-developed limit than in the entry region. The overall performances are controlled by the regions of the bundle having the lowest packing density (i.e., the highest porosity) and thus crossed by the highest flow rates: in these regions, the fluid residence times are lower than in the low porosity regions and the mass transfer coefficient dramatically decreases with respect to a regular fiber arrangement. Mass transfer coefficients for random distributions are only 5–10% (constant wall flux boundary condition) and ~15–25% (constant wall concentration) of the values for regular arrays. Moreover, while for regular arrays mass transfer coefficients exhibit a strong dependence on the bundle porosity (Cancilla et al., 2023), for random arrangements such dependence is very softened. These results suggest that bundles of random hollow fibers should not be used for applications operating in the ranges of low Graetz numbers.

In this work, the effects of the bundle non-uniformity are investigated by considering a model channel made up of low porosity and high porosity regions.

The paper is made up of two parts: the first one assumes that these regions are non-interacting and the flow and concentration fields are fully developed under an axial pressure gradient; this allows a simplified treatment of the problem. The second part considers three dimensional CFD simulations of fluid flow with mass transfer in a checkerboard arrangement of alternately high porosity and low porosity regions, each provided with a regular square array of fibers. This allows entry effects and the influence of region-to-region momentum and mass transfer to be taken into account.

2. Simplified treatment - non-interacting regions, fully developed conditions

If the flow and concentration fields are assumed to be fully developed and the regions of different porosity non-interacting, interesting results concerning the distribution of flow rates and mass transfer in a non-uniform bundle can be obtained from elementary considerations based on existing experimental or computational results for *uniform* bundles.

For simplicity, consider a generic porous channel of total cross sectional area A, filled with a fluid of viscosity μ and divided into two equal parts, characterized by local porosities ε_l ("loose") and ε_d ("dense") with $\varepsilon_l>\varepsilon_d$ (**Figure 2**).

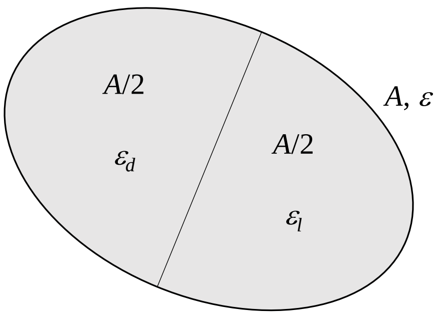

Figure 2: A generic porous channel divided into two regions with equal areas and different porosities.

The two porosities ε_l and ε_d can be expressed as functions of the mean porosity $\varepsilon=(\varepsilon_l+\varepsilon_d)/2$ and of the ratio $R_\varepsilon=\varepsilon_l/\varepsilon_d>1$:

$$\varepsilon_l = 2\frac{\varepsilon R_\varepsilon}{R_\varepsilon+1} \tag{1}$$

$$\varepsilon_d = 2\frac{\varepsilon}{R_\varepsilon + 1} \tag{2}$$

The mean porosity ε may only range between a minimum packing value ε_{min}, which depends on the lattice geometry and is ~0.21 for a square lattice and ~0.09 for a hexagonal lattice, and 1. Moreover, for any porosity ratio R_ε, ε is limited by the double constraint that the porosity ε_l of the "loose" region cannot exceed 1 and the porosity ε_d of the "dense" region cannot be less than ε_{min}, which leads to the double inequality:

$$\frac{\varepsilon_{min}}{2}\left(R_\varepsilon + 1\right) < \varepsilon < \frac{1}{2}\frac{R_\varepsilon + 1}{R_\varepsilon} \tag{3}$$

For example, for R_ε=2.25 and ε_{min}=0.21, Eq. (3) yields $0.341<\varepsilon<0.722$. Corresponding limitations apply to R_ε if the mean porosity ε is chosen.

Let us make the following hypotheses:

i) the flow is fully developed (this implies that there is no transverse flow and thus no advective scalar flux between regions at different porosity);

ii) there are no shear forces between the two regions (i.e. each of the two porous sub-channels behaves as if it were alone);

iii) each of the two regions of the porous medium follows Darcy's law with its own permeability *K*:

$$Q_l = \left|\frac{dp}{dz}\right|\frac{K_l}{\mu}\varepsilon_l\frac{A}{2} \tag{4}$$

$$Q_d = \left|\frac{dp}{dz}\right|\frac{K_d}{\mu}\varepsilon_d\frac{A}{2} \tag{5}$$

in which dp/dz is the pressure gradient along the direction of the channel's axis z, common to the two regions, while Q_l and Q_d are the flow rates.

For bundles of identical cylindrical fibers of diameter d, the permeability is a function of the porosity and of the fiber arrangement. In square and hexagonal regular lattices, CFD results for hydrodynamically fully developed flow were obtained by Cancilla et al. (2023) and are reported as symbols in **Figure 3**. In the range $\varepsilon\approx$0.21-0.90, the permeability for square lattices can be approximated with sufficient accuracy by the single exponential function, also shown in the figure:

$$\frac{K\varepsilon}{d^2} = 1.85\cdot 10^{-4}\exp\left(8.34\varepsilon\right) \tag{6}$$

The permeability for hexagonal lattices exhibits a more complex behavior and is not comparably easy to approximate with elementary functions.

Note that, by definition, in laminar parallel flow the Darcy permeability is independent from the Reynolds number, i.e. from the flow rate, as was verified by repeating some of the simulations leading to Eq. (6) at different Reynolds numbers <100.

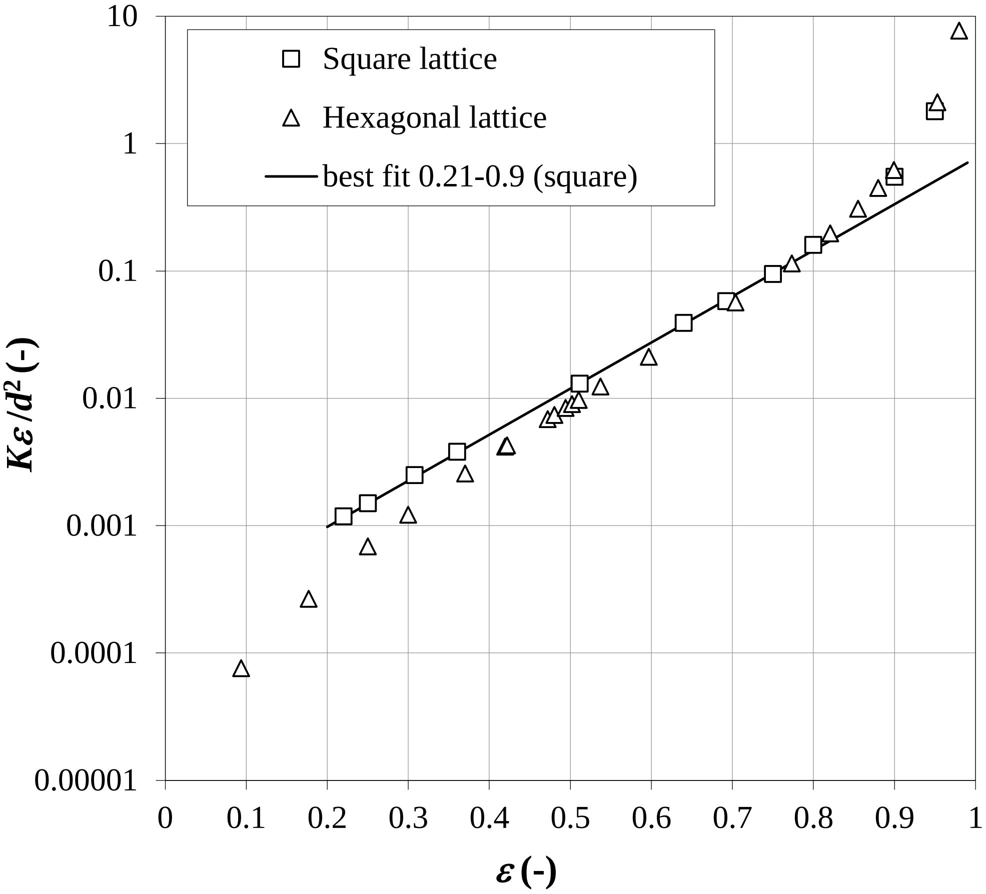

Figure 3: CFD results for the axial permeability K as a function of the porosity ε in regular square and hexagonal lattices. Permeabilities are made dimensionless as $K\varepsilon/d^2$. The exponential correlation for a square lattice in Eq. (6) is also shown.

By dividing Eq. (5) by Eq. (4) and taking account of Eqs. (1), (2) and (6), the flow rate ratio Q_l/Q_d is obtained:

$$\frac{Q_l}{Q_d} = \exp\left(16.68\varepsilon \frac{R_\varepsilon - 1}{R_\varepsilon + 1}\right) \tag{7}$$

Eq. (7) is represented in **Figure 4** and predicts the redistribution of the flow rates in the fiber bundle. Even moderate values of the porosity ratio $R_\varepsilon = \varepsilon_l/\varepsilon_d$ yield very large values of the flow rate ratio Q_l/Q_d; for example, for ε=0.5 and R_ε=2.25 one has $Q_l/Q_d \approx 25$. In **Figure 4**, the constraints in Eq. (3) are explicitly indicated.

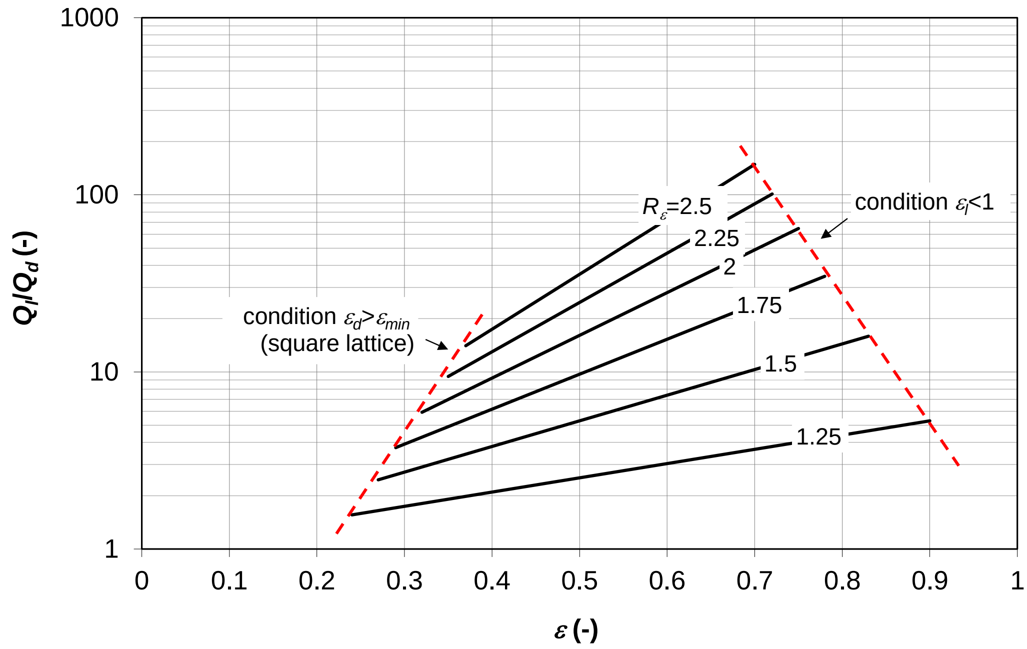

Figure 4: Flow rate ratio Q_l/Q_d as a function of the mean porosity ε for different values of the porosity ratio R_ε.

Another noteworthy quantity is the ratio Q_{tot}/Q_{unif} between the actual total flow rate $Q_{tot}=Q_d+Q_l$ across the whole section A (exhibiting non-uniform porosity) and the flow rate that would be obtained if the fibers were uniformly re-distributed across the section A, resulting in a uniform porosity $\varepsilon=(\varepsilon_l+\varepsilon_d)/2$.

Based on Eqs. (1)-(6), the actual total flow rate Q_{tot} can be expressed as

$$Q_{tot} = \left|\frac{dp}{dz}\right| \frac{Ad^2}{\mu} 8.75 \cdot 10^{-5} \left[\exp\left(16.68 \frac{\varepsilon R_\varepsilon}{R_\varepsilon + 1}\right) + \exp\left(16.68 \frac{\varepsilon}{R_\varepsilon + 1}\right) \right] \tag{8}$$

If the fibers were uniformly distributed with the mean porosity ε, the total flow rate would be

$$Q_{unif} = \left|\frac{\mathrm{d}p}{\mathrm{d}z}\right| \frac{Ad^2}{\mu} 1.75 \cdot 10^{-4} \exp(8.34\varepsilon) \tag{9}$$

Based on Eqs. (8) and (9), the ratio Q_{tot}/Q_{unif} can be expressed as a function of ε and R_ε as:

$$\frac{Q_{tot}}{Q_{unif}} = \frac{\exp\left(8.34\varepsilon \cdot \frac{2R_\varepsilon}{R_\varepsilon + 1}\right) + \exp\left(8.34\varepsilon \cdot \frac{2}{R_\varepsilon + 1}\right)}{2 \cdot \exp(8.34\varepsilon)} \tag{10}$$

Eq. (10) is represented in **Figure 5**. For example, for ε=0.5 and R_ε=2.25, one has Q_{tot}/Q_{unif}≈2.6. Thus, a non-uniform distribution of the fibers causes an increase of the overall (i.e., apparent) permeability and flow rate for any given pressure gradient.

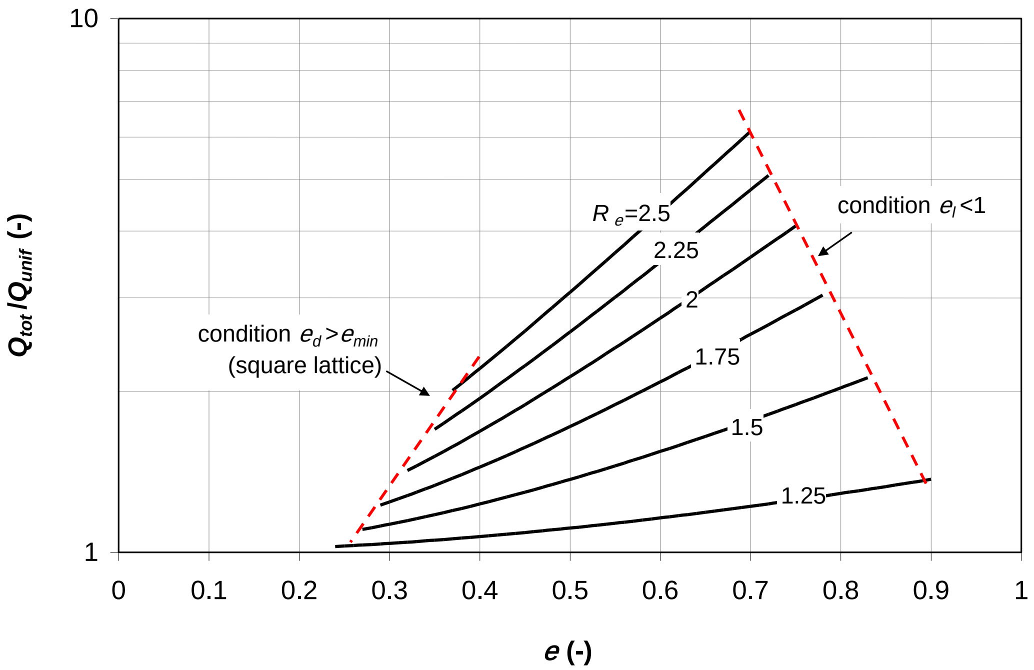

Figure 5: Flow rate ratio Q_{tot}/Q_{unif} as a function of the mean porosity ε for different values of the porosity ratio R_ε.

Similar considerations apply in regard to the transfer of a passive scalar (e.g., a solute's concentration). Besides assumptions (i)-(iii) above, let the following two also hold:

iv) the scalar field is also fully developed;

v) there are no diffusive scalar fluxes between the two regions (i.e. each of the two porous sub-channels behaves as if it were alone also from the point of view of scalar transfer).

Note that, as remarked above, the absence of *advective* scalar fluxes is implied by the assumption (i) of hydrodynamically fully developed flow.

A dimensionless mass transfer coefficient (Sherwood number Sh) for the transfer of a generic scalar of diffusivity D, based on the fibers' diameter d, can be defined for each region as

$$\mathrm{Sh}_r = \frac{\overline{j}_r}{\overline{C_{w,r}} - C_{b,r}} \cdot \frac{d}{D} \tag{11}$$

where r=d ("dense") or l ("loose"), $\overline{j}_r$ and $\overline{C_{w,r}}$ are the wall scalar flux and species concentration at the wall, averaged over the fibers' perimeter (fiber-fluid interface) in region "r", and $C_{b,r}$ is the bulk concentration in region "*r*", defined as the mass flow – weighted average of the species concentration on a cross section of region "*r*".

CFD results for regular square and hexagonal arrays of cylindrical fibers in fully developed flow and concentration fields under boundary conditions of constant wall mass flux j or constant wall concentration C_w are reported in **Figure 6**. Results for constant j have already been reported in a previous paper (Cancilla et al., 2023) and are in excellent agreement with the CFD results presented by Bao and Lipscomb (2002a). Results for constant C_w (unpublished so far) do not completely agree with those presented by Bao and Lipscomb (2002b), which exhibit lower values of Sh at low and intermediate porosities.

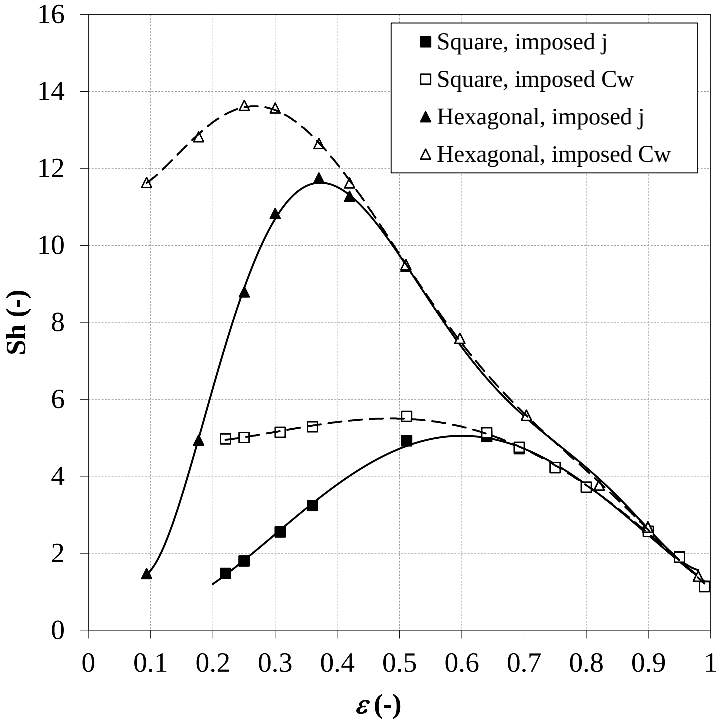

Figure 6: Sherwood number as a function of the mean porosity ε for regular square and hexagonal fiber arrays under conditions of constant wall mass flux j and constant wall concentration C_w. Symbols: CFD results; lines: best-fit polynomial curves.

The results can be approximated by suitable functions (6th-order polynomials were used here for the calculations that follow). All curves exhibit a maximum at some intermediate ε and low values for very small or very large porosities. For the square array, the maximum occurs at $\varepsilon \approx 0.60$ (constant j) or ~0.50 (constant C_w); for the hexagonal array, the maximum occurs at $\varepsilon \approx 0.37$ (constant j) or ~0.25 (constant C_w). In the whole porosity range and for both boundary conditions, Sh is larger for hexagonal than for square arrays, the difference decreasing at large ε.

For both geometries, Sh is larger under constant-C_w than under constant-j boundary conditions at low ε, while the boundary conditions become irrelevant for ε larger than a certain value (~0.65 for the square lattice and ~0.5 for the hexagonal one). This behavior is opposite to that observed in plane channels and circular pipes, in which uniform-j boundary conditions yield *larger* values of Sh.

Under the present parallel flow conditions, the Sherwood number is independent both from the Reynolds number (flow rate), as was verified by repeating some of the simulations reported in **Figure 6** for different Reynolds numbers <100, and from the Schmidt number, as was verified by comparing results for Sc=1 and 500.

The results in **Figure 6** can be used to compute the ratio Sh_l/Sh_d of the Sherwood numbers occurring in the two, "loose" and "dense", halves of the channel for any realizable combination of the mean porosity ε and the porosity ratio R_ε. For the case of a square lattice and constant wall mass flux, the results are represented in **Figure 7**. Note that all curves are limited by the two constraints $\varepsilon_d>\varepsilon_{min}$ and $\varepsilon_l<1$. It can be observed that a critical porosity value $\varepsilon_c\approx 0.6$ exists, such that for $\varepsilon<\varepsilon_c$ the Sherwood number is larger in the "loose" region of the channel, whereas the opposite is true for $\varepsilon>\varepsilon_c$. For example, for ε=0.5 and R_ε=2.25, one has $Sh_l/Sh_d\approx 1.85$.

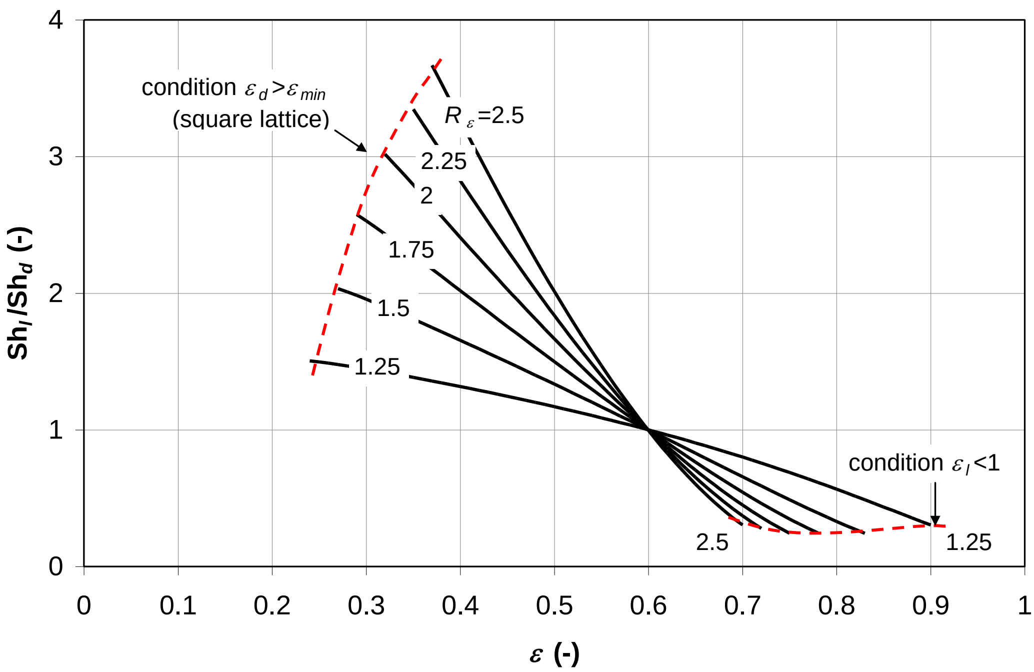

Figure 7: Sherwood number ratio Sh_l/Sh_d as a function of the mean porosity ε for different values of the porosity ratio R_ε (square lattice, constant wall scalar flux).

A second noteworthy quantity is the ratio Sh/Sh_{unif} between the overall (also called mean, or apparent) Sherwood number Sh in the non-uniform channel and the Sherwood number Sh_{unif} that would be obtained if the fibers were uniformly re-distributed, resulting in a uniform porosity $\varepsilon=(\varepsilon_l+\varepsilon_d)/2$.

The Sherwood number Sh_{unif} in the denominator can simply be obtained from polynomial approximations of the results in **Figure 6**.

The numerator (mean Sherwood number Sh in the two-region non-uniform channel) can be evaluated from Eq. (11) by omitting the subscript "*r*", i.e., computing the mean mass flux $\overline{j}$ and the mean wall concentration $\overline{C_w}$ over all the fibers, and the bulk concentration C_b over the whole cross section *A*.

Considering, for simplicity, only the case of uniform wall mass flux *j*, the mean mass flux obviously is $\overline{j} = j$.

The partial flow rates Q_d and Q_l are given, for any pressure gradient and viscosity, by Eqs. (1) and (2) in which the Darcy permeabilities can be expressed using Eq. (6). The bulk concentration in either region "*r*" is then given by a scalar balance from *z*=0 to the generic axial location *z* by:

$$C_{b,r} = C_0 + \frac{\pi d N_r jz}{Q_r} \tag{12}$$

where C_0 is the inlet concentration, which is irrelevant for the present purposes and will be assumed to be zero, while N_r is the number of fibers in either region, which can be expressed as

$$N_r = \frac{(1-\varepsilon_r)(A/2)}{\pi d^2/4} \tag{13}$$

The mean bulk concentration, being the mass-flow-weighted average of the local concentration, can be computed as

$$C_b = \frac{C_{b,d}Q_d + C_{b,l}Q_l}{Q_d + Q_l} \tag{14}$$

The evaluation of the mean wall concentration $\overline{C_w}$ is more cumbersome because it requires the partial averages of C_w over the "dense" and "loose" regions, $\overline{C_{w,d}}$ and $\overline{C_{w,l}}$. However, these can be evaluated starting from the partial Sh_d and Sh_l values computed for each porosity by using the results in **Figure 4** and then inverting Eq. (11) to obtain, for either region "*r*":

$$\overline{C_{w,r}} = C_{b,r} + \frac{j}{\mathrm{Sh}_r} \cdot \frac{d}{D} \tag{15}$$

Finally, the overall average of C_w can be obtained as a weighted average over the fiber perimeters, proportional to their numerosity:

$$\overline{C_w} = \frac{C_{w,d} N_d + C_{w,l} N_l}{N_d + N_l} \tag{16}$$

Once j, $\overline{C_w}$ and C_b are known, Eq. (11) can be used to obtain the overall Sherwood number in the non-uniform bundle.

For example, consider a square lattice with ε_d=0.31, ε_l=0.69 (mean porosity ε=0.5) and assume d=280·10^{-6} m, z=0.2 m, A=12.56·10^{-4} m^2, j=1·10^{-5} mol/(m^{2}s) (uniform), |dp/dz|=4·10^3 Pa/m, μ=10^{-3} Pa·s, ρ=10^3 kg/m^3, Sc=500 so that D=μ/(ρSc)=2·10^{-9} m^2/s (these latter data are roughly representative of a hemodialyzer).

From the results in Figure 4, the Sherwood number in a regular square lattice with ε=0.5 would be $\mathrm{Sh}_{unif}\approx$4.84.

From Eq. (6) one has K_d=4.38·10^{-10} m^2, K_l=6.49·10^{-9} m^2. From Eqs. (1) and (2) one has Q_d=3.41·10^{-7} m^3/s (20.46 ml/min), Q_l=11.04·10^{-6} m^3/s (674.8 ml/min), so that Q_{tot}=11.58·10^{-6} m^3/s (695.4 ml/min). From Eq. (13) one has N_d=7037, N_l=3162 so that Eq. (12) yields bulk concentrations $C_{b,d}$=36.31 mol/m^3, $C_{b,l}$=0.50 mol/m^3 and Eq. (14) yields a "grand" mean bulk concentration C_b=1.55 mol/m^3. From the curve in Figure 5 relative to a square lattice with constant j (or from the relevant polynomial approximation) one has $\mathrm{Sh}_d\approx$2.5 for ε=0.31 and $\mathrm{Sh}_l\approx$4.6 for ε=0.69. Therefore, Eq. (15) yields for the mean wall concentrations $\overline{C_{w,d}}\approx$36.87 mol/m^3, $\overline{C_{w,l}}\approx$0.81 mol/m^3 while Eq. (16) yields a "grand" mean wall concentration $\overline{C_w}\approx$25.69 mol/m^3. Finally, Eq. (11) yields Sh=0.058 for the overall Sherwood number (note that this value is much less than either Sh_d or Sh_l) so that the $\mathrm{Sh}/\mathrm{Sh}_{unif}$ ratio is 0.058/4.84≈0.012 (i.e., Sh is almost two orders of magnitude less than Sh_{unif}).

This procedure can be repeated for different values of the two porosities with the help of a spreadsheet. The resulting $\mathrm{Sh}/\mathrm{Sh}_{unif}$ ratio for the case of a square lattice and constant wall mass flux is represented in **Figure 8** as a function of the mean porosity ε for different values of the porosity ratio R_ε. Note that a logarithmic scale had to be used for the $\mathrm{Sh}/\mathrm{Sh}_{unif}$ ratio because of the broad range spanned by this quantity, and that the constraints in Eq. (3) have been represented.

Under most of the realizable conditions considered, the $\mathrm{Sh}/\mathrm{Sh}_{unif}$ ratio is <1, decreases with increasing R_ε, i.e. with increasing non-uniformity, and attains minimum values below 0.01. For example, for ε=0.5 and R_ε=2.25 one has $\mathrm{Sh}/\mathrm{Sh}_{unif}\approx$0.012. Such extremely low values of Sh in non-uniform bundles are somewhat surprising, but are actually in agreement with the results of Lipscomb and co-workers (Bao and Lipscomb, 2002a, 2002b) for random arrays of fibers, exhibiting a comparable amount of non-uniformity.

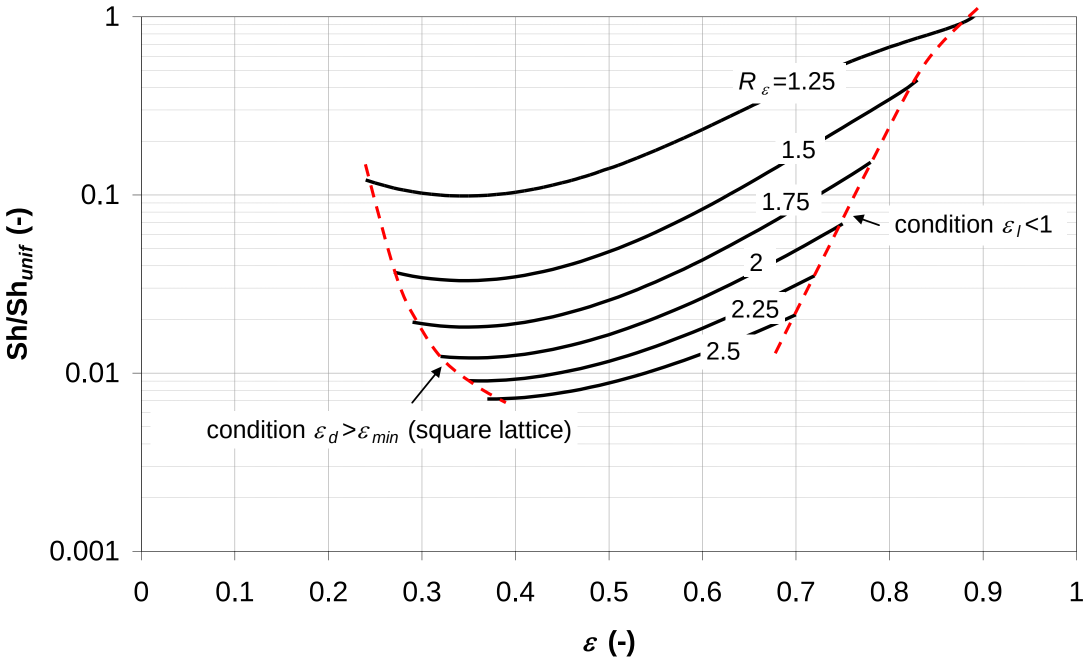

Figure 8: Sherwood number ratio Sh/Sh_{unif} as a function of the mean porosity ε for different values of the porosity ratio R_ε (square lattice, constant wall scalar flux).

The results in this Section can be summarized by stating that introducing non-uniformity in the distribution of porosity over the cross section of a channel, while preserving the mean porosity, causes an increase of the overall permeability and a large decrease of the mass transfer coefficient (Sherwood number) with respect to the uniform porosity case.

The above results were obtained under assumptions (i)-(v), and in particular for

- fully developed flow and concentration fields;
- no interaction between the “dense” and “loose” regions in terms of exchanged shear forces and diffusive mass fluxes,

so that they strictly apply only to the limiting case of an infinitely long channel with “dense” and “loose” regions of infinite cross-sectional area (i.e., surface-to-volume ratio $\rightarrow$ 0).

Accounting for the finite size of the different regions (i.e., for the length scale of the non-uniformity) and for entrance effects requires that the elementary one-dimensional approach of this Section has to be replaced by a more complete treatment, involving the use of Computational Fluid Dynamics. This will be done in the next Section.

3. CFD treatment - interacting regions, developing conditions

3.1 Computational domain

The aim of this Section is to investigate the influence of the extent and spatial scale of the non-uniformity in the fiber distribution in a bundle and to clarify the influence of non-uniformity on entrance effects and development lengths. To this purpose, an “artificial” cross section geometry was built, composed of alternate square regions of higher and lower porosity, arranged in a checkerboard pattern. In each region, the fibers were assumed to be arranged in a square lattice. For symmetry reasons, it was sufficient to include in the computational domain only two low-porosity (“dense”) and two high-porosity (“loose”) square regions while imposing lateral periodicity at the opposite sides.

An example of the resulting computational domain is shown in **Figure 9**.

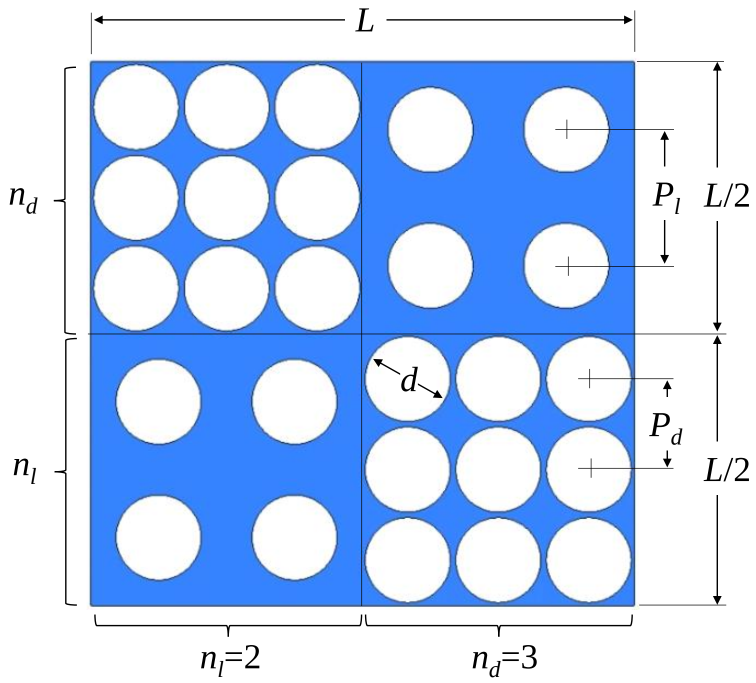

Figure 9: Cross section of a computational domain representing a fiber bundle divided into “dense” and “loose” regions arranged in a checkerboard pattern. In the example shown (“small” geometry with 2×2 and 3×3 fibers), one has ε=0.5, ε_l=0.69, ε_d=0.31; the domain includes 26 fibers.

In order to establish its geometry, the first step is to choose a mean porosity ε and two small different integer numbers n_d (for “dense”) and n_l (for “loose”). The numbers of fibers in the “dense” and “loose” regions are $N_d=2n_d^2$ and $N_l=2n_l^2$, respectively, and the overall number of fibers in the computational domain (square of side length L) is $N_{tot}=N_d+N_l$.The two porosities ε_l, ε_d are obtained by considering the two identities

$$\frac{\varepsilon_l + \varepsilon_d}{2} = \varepsilon \tag{17}$$

$$\frac{1-\varepsilon_d}{1-\varepsilon_l} = \left(\frac{n_d}{n_l}\right)^2 \tag{18}$$

which yield

$$\varepsilon_d = \frac{1-\left(1-2\varepsilon\right)\left(n_d / n_l\right)^2}{1+\left(n_d / n_l\right)^2} \tag{19}$$

$$\varepsilon_l = \frac{\left(n_d / n_l\right)^2 - \left(1-2\varepsilon\right)}{1+\left(n_d / n_l\right)^2} \tag{20}$$

and thus the porosity ratio $R_\varepsilon = \varepsilon_l/\varepsilon_d$.

The pitches (center-center distances between adjacent fibers) are now obtained by imposing the conditions, valid in each unit cell:

$$\frac{P_l^2 - \pi d^2/4}{P_l^2} = \varepsilon_l \tag{21}$$

$$\frac{P_d^2 - \pi d^2/4}{P_d^2} = \varepsilon_d \tag{22}$$

which yield

$$P_l = \frac{d}{2}\sqrt{\frac{\pi}{1-\varepsilon_l}} \tag{23}$$

$$P_d = \frac{d}{2}\sqrt{\frac{\pi}{1-\varepsilon_d}} \tag{24}$$

Finally, the side length of each square region is $L/2=n_lP_l=n_dP_d$.

In the example in **Figure 9** (“small” geometry), the values 2 and 3 were chosen for n_l and n_d and the value 0.5 for the mean porosity ε. The above formulae yield ε_l=9/13≈0.6923…, ε_d=4/13≈0.3077…, R_ε=(9/13)/(4/13)=2.25, P_l≈1.5977·d, P_d≈1.0651·d, $L/2$≈3.1954·d, N_l=2×(2×2)=8, N_d=2×(3×3)=18. Thus, the whole computational domain includes N_{tot}=26 fibers.

For a mean porosity ε of 0.5, the choice n_l=2 and n_d=3 yield the simplest possible computational domain. The only couple of smaller numbers (n_l=1, n_d=2) would yield, based on Eqs. (19)-(20), ε_l=4/5 and ε_d=1/5; but this latter value is smaller than the minimum realizable porosity in a square lattice (~0.21).

The same values of ε, ε_l, ε_d, P_l and P_d can be obtained multiplying n_l, n_d by the same integer number. This property can be exploited to build larger computational domains and was used in the present paper to investigate the influence of the spatial scale of the non-uniformity in the porosity distribution. For example, **Figure 10** shows the case n_l=4, n_d=6 ("large" geometry), for which the side length of each region is double with respect to the example in **Figure 9**; of course, the cross sectional areas and the numbers of fibers (104) are four times larger.

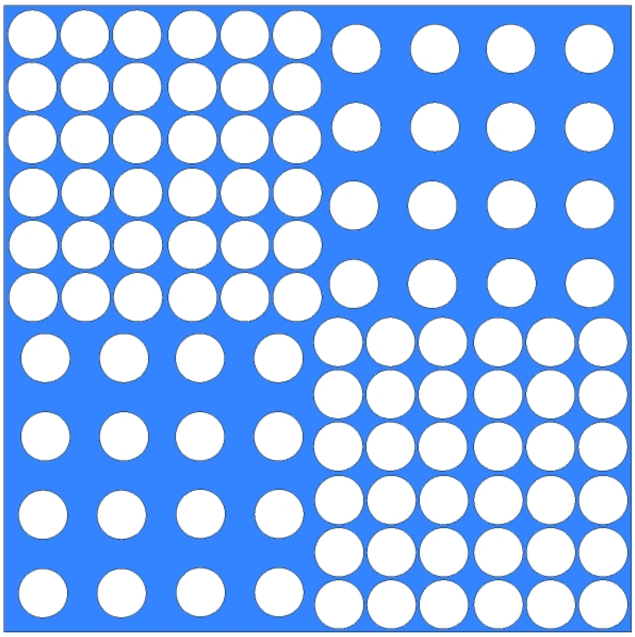

Figure 10: Cross section of a computational domain representing a fiber bundle divided into "dense" and "loose" regions arranged in a checkerboard pattern. In the example shown ("large" geometry), the domain includes 2×(4×4)+2×(6×6)=104 fibers.

For a Schmidt number of 1, the extent of the computational domain along the axial direction z was set to ~900d, a length amply sufficient to achieve fully developed hydrodynamics and mass transfer thus elucidating entry effects. For Sc=500, on the basis of the Graetz-Leveque theory of entrance effects (Everts and Meyer, 2020), comparably developed conditions would be achieved only after a distance of the order of 500×900d=450,000d from the inlet, which, however, is computationally prohibitive. Thus, the length of the computational domain was actually limited to 36,000d (corresponding to a physical length of ~10 m for d=280·10^{-6} m), just sufficient to attain axial mass transfer development for a Reynolds number of 10 as will be shown below.

3.2 Definitions

The axial interstitial velocity $\langle w \rangle$ is defined as the area average of the local velocity component w along the axial direction z, performed over the area occupied by the fluid. In particular, $\langle w \rangle_d$ is the interstitial velocity obtained by averaging w over the "dense" region and, similarly, $\langle w \rangle_l$ is the interstitial velocity obtained by averaging w over the "loose" region.

The axial interstitial Reynolds number of the "dense" (subscript $r=d$) or "loose" regions (subscript $r=l$) Re_r, based on the fiber diameter d, is defined as

$$\mathrm{Re}_r = \frac{\rho \langle w \rangle_r d}{\mu} \tag{25}$$

The axial interstitial Darcy hydraulic permeability K_r is defined as:

$$K_r = \frac{\mu \langle w \rangle_r \varepsilon_r}{\left| \mathrm{d}p/\mathrm{d}z \right|_r} \tag{26}$$

where ε_r is the porosity of the "dense" ($r=d$) or "loose" ($r=l$) region; the only difference with respect to the implicit definition of permeability given in Section 2, Eqs. (1) and (2), is that now the possibility of different axial pressure gradients in the two regions is taken into account, as it is appropriate in the entrance (development) region of the channel.

The Sherwood number in the "dense" or "loose" region is still defined by Eq. (11).

3.3 Governing equations and boundary conditions

The following steady-state continuity and momentum equations for the flow of a Newtonian incompressible fluid, along with the convection-diffusion equation governing the transport of a passive scalar (e.g. a solute concentration), were used:

$$\vec{\nabla} \cdot \vec{u} = 0 \tag{27}$$

$$\rho \vec{u} \cdot \vec{\nabla} \vec{u} = -\vec{\nabla} p + \mu \nabla^2 \vec{u} \tag{28}$$

$$\vec{u} \cdot \vec{\nabla} C = D \nabla^2 C \tag{29}$$

in which $\vec{u}$ is the local velocity, p is the local pressure, ρ and μ are the density and dynamic viscosity of the fluid, C and D are the local concentration and the kinematic diffusivity of the scalar in the fluid.

The above equations were solved by using the finite volume code ANSYS-CFX 18® (ANSYS, 2018). The fluid properties were set equal to those of water at 25°C. The study was conducted for

Schmidt numbers Sc=$\mu/(\rho D)$ of 1, representative of heat transfer in gases and other common fluids, or 500, better representative of mass transfer of many species in water.

Regarding hydrodynamics, the cylindrical surfaces representing the fibers' walls were treated as no slip walls. At the inlet a uniform interstitial velocity was imposed, set to a value that guarantees a mean interstitial Reynolds number of 20 (averaging over "loose" and "dense" regions), while at the outlet the pressure was arbitrarily set to zero.

Regarding mass transfer, in most cases a Neumann boundary condition was adopted, with an arbitrarily set value for the scalar flux. In some cases, Dirichlet boundary conditions were also tested, with the concentration at the walls set at an arbitrary uniform value. Without any loss of generality, the inlet concentration was arbitrarily set to zero.

The fluid flow and concentration fields started from an initial guess of zero velocity and zero concentration. Periodic boundary conditions were imposed to all quantities at the opposite side surfaces of the fluid domain along the *x* and the *y* directions, respectively. **Figure 11** shows the boundary conditions employed for a test case corresponding to the "large" domain in **Figure 10**.

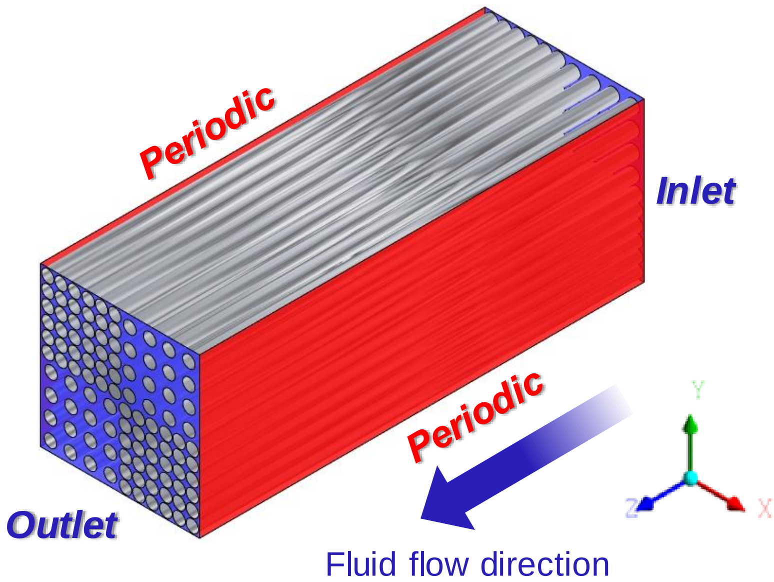

Figure 11: Computational domain ("large" geometry) and boundary conditions used in the simulations. For representation purposes, the domain is shown compressed many times along *z*.

3.4 Domain discretization and computational methods

The computational domain was discretized by hybrid grids made up of hexahedral and wedge volumes. The use of hybrid meshes was necessary because of the complexity of the geometries considered, which are difficult to be meshed by hexahedra only. However, all the grids used are mostly composed of hexahedral volumes, as summarized in **Table 1**.

Table 1: Summary of the grids employed.

Geometry	Number of finite volumes	% of volume discretized with hexahedra
small	~6,300,000	99.5
large	~28,500,000	99.3

Figure 12 shows details of the mesh in a cross section of the "loose" and "dense" regions.

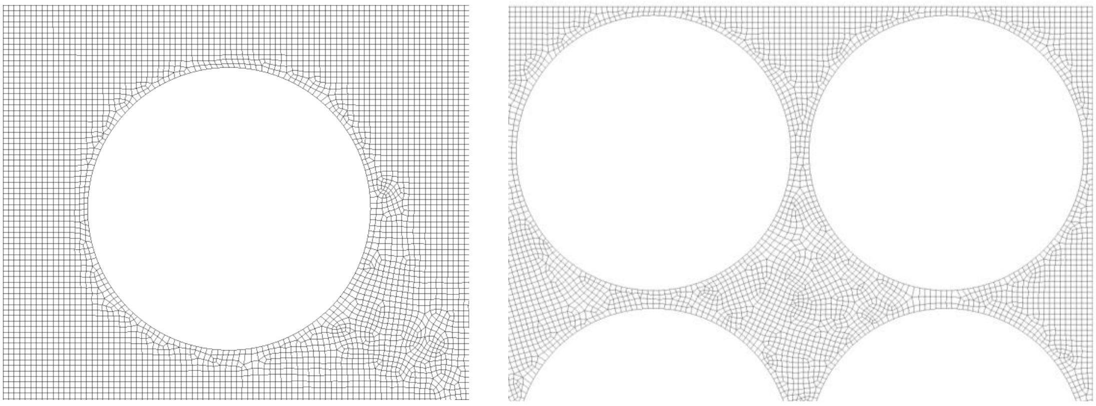

(a) (b)

Figure 12: Details of the mesh over a cross section of the computational domain. (a) "loose" region (b); "dense" region.

Along the axial direction *z*, the computational domains were discretized in all cases by 110 finite volumes, which were selectively refined towards the inlet.

A full grid-independence study was unfeasible for the present geometries due to the large number of fibers. Based on a previous grid-independence assessment for a unit cell including a single fiber (Cancilla et al., 2021), the present grid resolution (~2500 finite volumes per fiber in the cross sectional plane) implies a discrepancy of ~5% on the axial Darcy permeability and of less than 1% on the Sherwood number. Therefore, the present results can *not* be regarded as grid-independent, especially from the hydrodynamic point of view; however, they are acceptable as far as the *difference* in Darcy permeability and Sherwood number between regions at different porosity is the main point at issue.

All simulations were run in double precision and were interrupted as the dimensionless residuals of all quantities decreased below 10^{-12}, which is a very tight convergence criterion. A two-point upwind scheme was used for the discretization of the advection terms. A strongly coupled algorithm was adopted to solve for pressure and velocity. A different number of iterations, in the form of false time steps, was used for the present steady state simulations depending on flow rate, system geometry and boundary conditions.

3.5 CFD Results

3.5.1 Hydrodynamics

Figure 13 shows velocity contour plots at $z/d \approx 900$ (hydrodynamically fully developed conditions) for the two geometries simulated and a mean interstitial Reynolds number of 20. Note that the same scale is used for both maps.

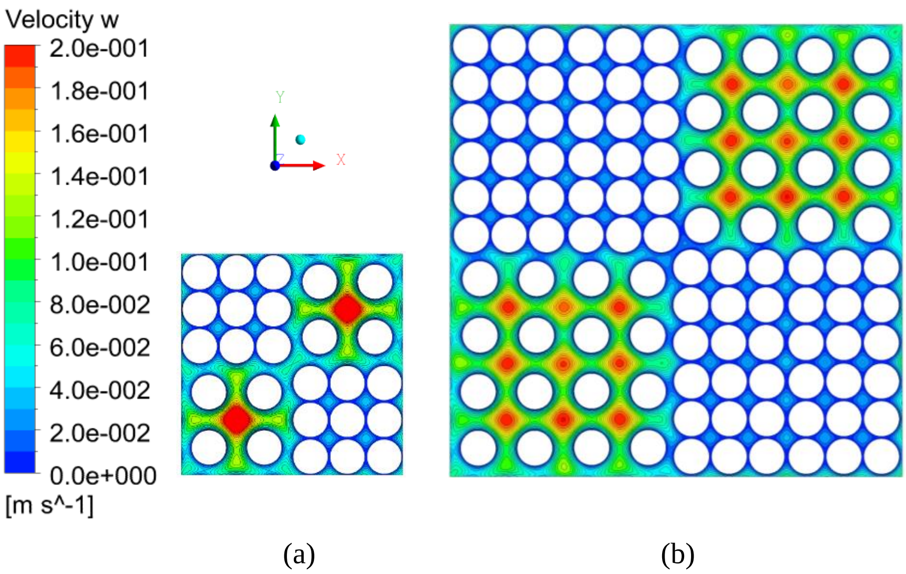

Figure 13: Contour plots of the axial velocity over cross sections of the computational domains lying in the hydrodynamically fully developed region: (a) “small” geometry; (b) “large” geometry.

In all cases, the “dense” regions are characterized by lower velocities while the peak values are reached in the “loose” regions, thus implying the flow rate redistribution between regions of different local porosity, as already observed by other authors (Bao and Lipscomb, 2002b; Sangani and Yao, 1988).

In the fully developed flow region, the “loose” to “dense” flow rate ratio attains a value of ~8.7 for the “small” geometry and of ~11.6 for the “large” one. These values are much lower than that of 34.33 predicted by Eq. (7) for the present porosities of ~0.69 and ~0.31, and the largest discrepancy is obtained with the “small” geometry. This discrepancy is due to the fact that Eq. (7) is for infinite (non-interacting) “dense” and “loose” regions, whereas the interaction between regions at different porosity, mainly by lateral diffusion of axial momentum (shear forces), is fully taken into account by the CFD simulations and tends to equalize the two flow rates. These results show that this interaction is quite strong even for the "large" geometry ($L \approx 12.78 \cdot d$), and that a much larger scale of the non-uniformity would be required for the flow rate ratio closely to approach that predicted by Eq. (7).

The better to highlight the influence of the length scale of the non-uniformity, **Figure 14** reports the fully developed longitudinal Darcy permeability K (normalized by d^2) as a function of the scale L (normalized by d). Dashed lines represent the asymptotic values of the axial fully developed Darcy permeabilities predicted for infinite regular square lattices (red for the "dense" porosity of ~0.31, blue for the "loose" porosity of ~0.69, black for the mean porosity of 0.5). Symbols and solid lines represent the fully developed axial Darcy permeabilities K_d and K_l computed by the present CFD simulations for the "small" and "large" geometries, corresponding to L/d=6.39 and 12.78, respectively.

In non-uniform array of fibers, the "dense" and "loose" fully developed permeabilities depart from the value for ε=0.5, approaching the values for uniform bundles of the corresponding porosity, the more as the length scale of the non-uniformity increases. In particular, in the "small" geometry, simulations predict K/d^2=1.18×10^{-2} and 4.62×10^{-2}, respectively for the "dense" and the "loose" regions, while for the "large" geometry these values become 1.13×10^{-2} and 6.10×10^{-2}.

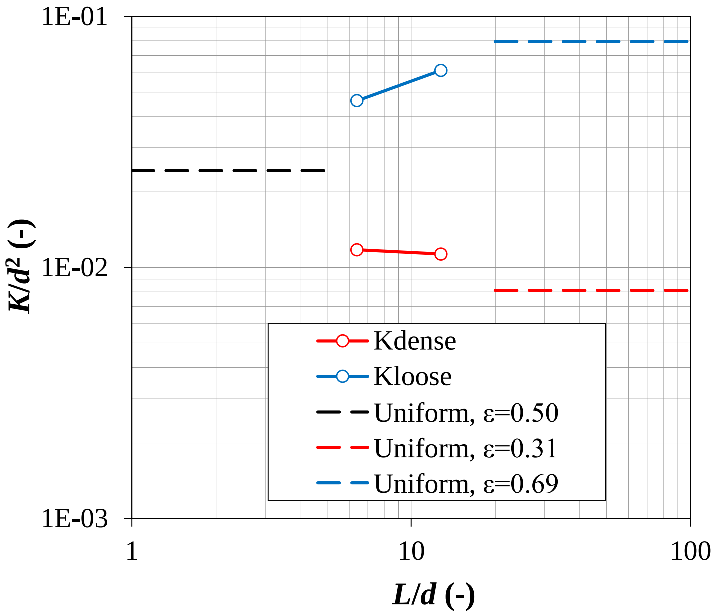

Figure 14: Fully developed axial Darcy permeability K (normalized by d^2) as a function of the length scale of the non-uniformity (normalized by d).

In order to show the influence of non-uniformity on hydrodynamic entrance effects, **Figure 15** reports the Darcy permeability K, normalized by its fully developed value K_∞, as a function of the dimensionless distance from the inlet, z/d, for the "dense" ($\varepsilon \approx 0.31$, graph a) and "loose" ($\varepsilon \approx 0.69$, graph b) regions of both geometries (small and large domains) and as the "grand" average between "dense" and "loose" regions (graph c). In each plot, K/K_∞ profiles are compared with that predicted for an infinite uniform square array of fibers of the corresponding porosity.

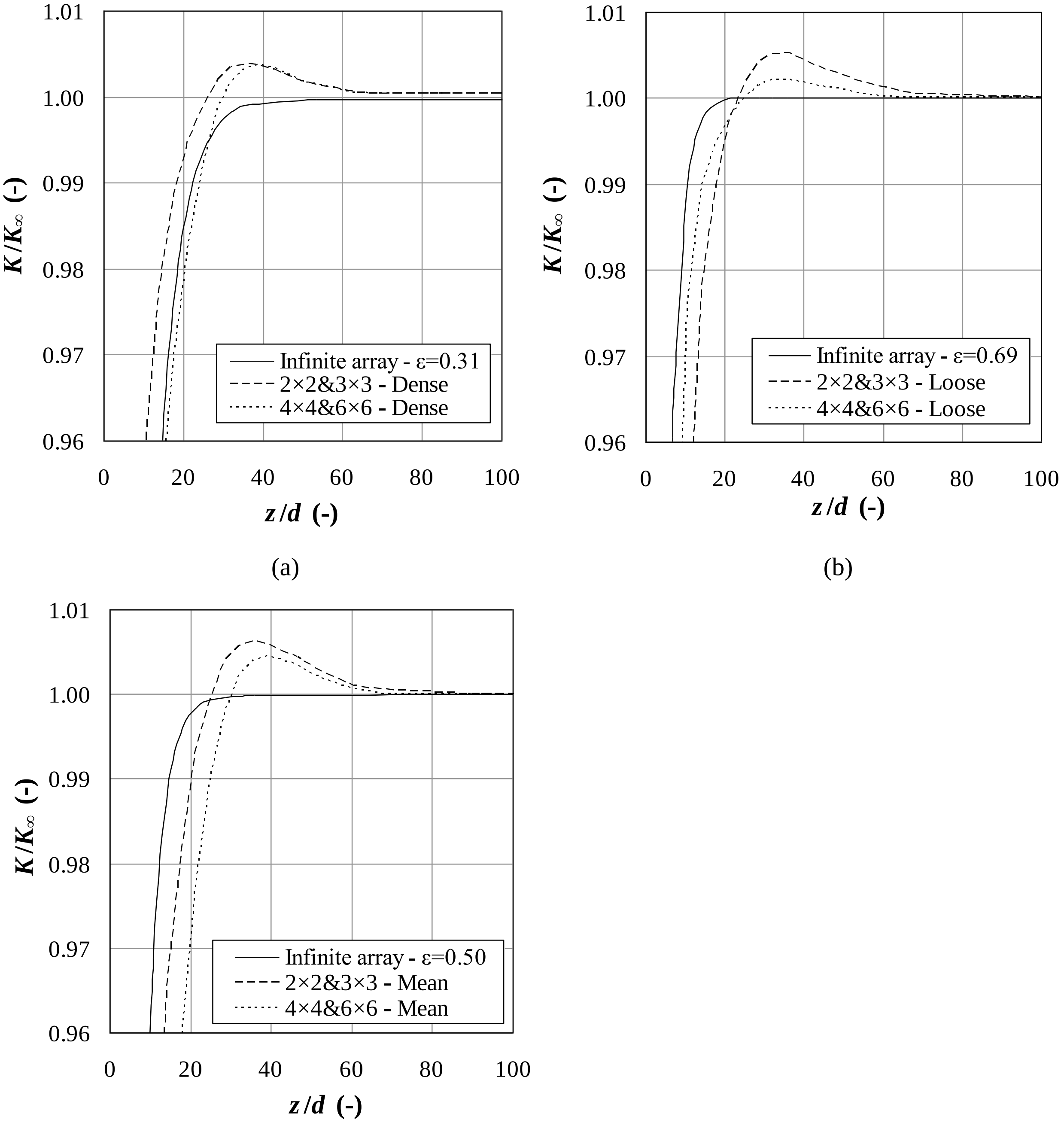

(a) (b)

(c)

Figure 15: Darcy permeability K as a function of the dimensionless axial coordinate z/d for both the geometries investigated ("small", i.e. 2×2&3×3 fibers, and "large", or 4×4&6×6 fibers), along with the results for infinite square lattices of uniform porosity. The permeability is made dimensionless as K/K_∞. Porosity: (a) ε=0.31; (b) ε=0.69; (c) ε=0.50.

In the uniform-porosity cases, the permeability increases monotonically tending to its asymptotic value (of course, this behaviour is opposite to that of the friction coefficient, which diverges for $z \to 0$). The dimensionless hydrodynamic development length $z_{h,dev}/d$, as identified, for example, by the condition $|K-K_\infty|/K_\infty<0.01$ (1% criterion), decreases from ~23 to ~14 and ~10 as the porosity increases from 0.31 to 0.5 and 0.69.

In the non-uniform porosity geometries, K/K_∞ exhibits a quite different behaviour, attaining a maximum before relaxing towards its asymptotic (fully developed) value. By the 1% criterion, the development length is not much different from that for a uniform geometry, and is not even always larger; for example, for the "dense" region of the "small" geometry one has $z_{h,dev}/d \approx 19$ against the value $z_{h,dev}/d \approx 23$ holding for a uniform bundle of the same porosity $\varepsilon=0.31$, see **Figure 15**(b). However, if a tighter convergence of K to its asymptotic value K_∞ is imposed to define $z_{h,dev}$, then it becomes significantly larger in non-uniform geometries than in uniform ones; for example, the condition $|K-K_\infty|/K_\infty<0.001$ (1‰ criterion) is attained (from below) for $z_{h,dev}/d \approx 35$ in a uniform array with $\varepsilon=0.50$, but is attained (from above) only for $z_{h,dev}/d \approx 60$-70, i.e. about twice farther downstream, in both the "small" and the "large" non-uniform geometries when the mean permeability is considered, see **Figure 15**(c).

3.5.2 Mass transfer

The bulk concentrations in the "dense" and "loose" regions ($C_{b,d}$ and $C_{b,l}$, respectively) vary along the axial direction z according to the following balance equations

$$Q_d \frac{\mathrm{d}C_{b,d}}{\mathrm{d}z} = \pi d N_d j_d - 2L j_{d\to l} \tag{30}$$

$$Q_l \frac{\mathrm{d}C_{b,l}}{\mathrm{d}z} = \pi d N_l j_l + 2L j_{d\to l} \tag{31}$$

in which Q_d and Q_l are the flow rates in the two regions, N_d and N_l are the numbers of fibers (so that $\pi d N_r$ is the fiber perimeter in the generic region "r", i.e. either "d" or "l"), j_d and j_l are the mean scalar fluxes at the fibers' walls (imposed to be uniform and equal to j in the present simulations), $L/2$ is the side length of each sub-region (so that $4L/2=2L$ is its boundary perimeter) and $j_{d\to l}$ is the average scalar flux from the "dense" region at higher concentration to the "loose" region at lower concentration. Note that $j_{d\to l}$ includes an advective contribution (which tends to zero for increasing z, when cross flows vanish and the fluid's motion becomes parallel) and a diffusive contribution (which depends only on the concentration difference between "dense" and "loose" regions).

For distances z from the inlet larger than a certain mass transfer development length $z_{dev,C}$, the flow rates Q_d and Q_l, the flux $j_{d\to l}$ and the difference C_d-C_l all become constant. This is clearly shown by the behaviour of the “dense” and “loose” bulk concentrations for a Schmidt number of 1, reported in **Figure 16**. Larger length scales *L* yield larger asymptotic differences between “dense” and “loose” bulk concentrations, clearly due to the weaker coupling between adjacent regions at different porosity.

The value of $z_{dev,C}$ depends on its exact definition, on the Schmidt number and on the length scale *L* of the non-uniformity. For Sc=1, it is ~200*d* for the “large” geometry and ~100*d* for the “small” one when defined as the length beyond which the difference in concentration between regions attains within 1% its asymptotic value. Thus, it is larger than the 1% hydrodynamic development length defined above.

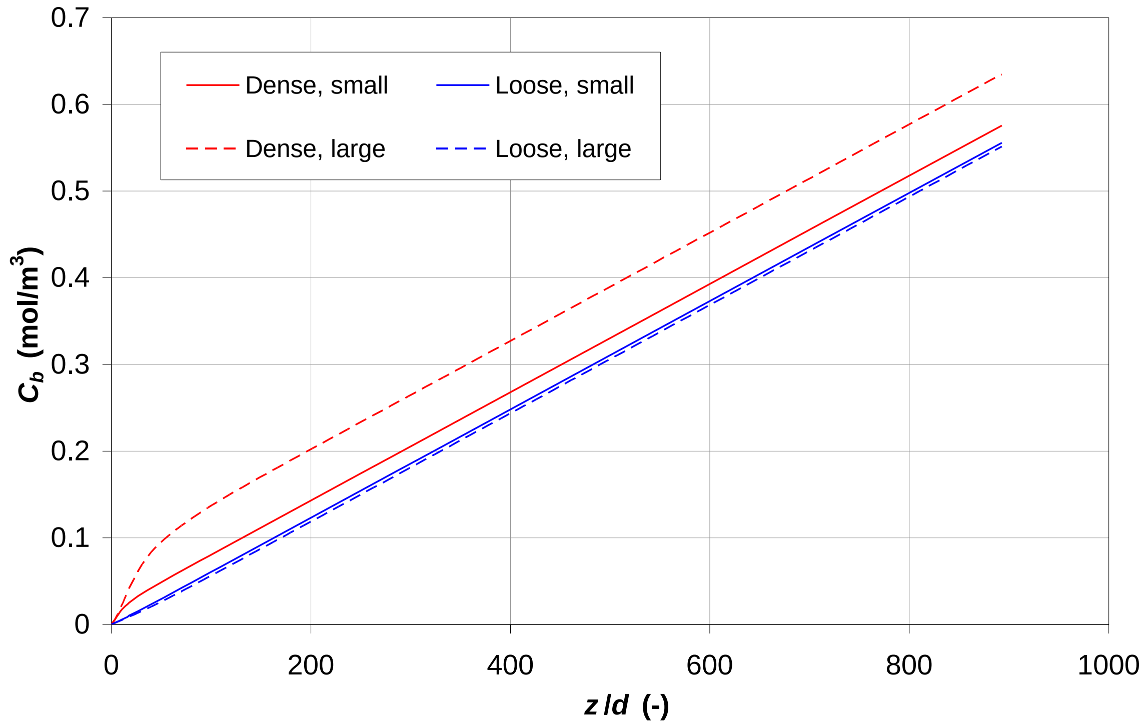

Figure 16: Bulk concentration in the “dense” and the “loose” regions of the bundle as a function of the dimensionless axial coordinate *z*/*d* at Sc=1 for the two geometries simulated.

Figure 17 reports concentration contour plots at *z*/*d*≈900 (well into the fully developed scalar transfer region) for the two geometries investigated and a Schmidt number of 1. The quantity shown is the difference C-C_b between the local concentration *C* and the overall bulk concentration C_b computed over the whole cross section, which includes both the “dense” and the “loose” regions.

The “dense” regions, where the fluid flows with the lower velocities, are characterized by higher concentrations and *vice versa*. Unlike in **Figure 13**, maps are reported with different scales because the concentration variance is much larger in the larger geometry.

The “small” geometry (a) shows maxima of C-C_b of ~$4\cdot10^{-2}$ mol/m^3 in the “dense” regions and minima of ~$-1\cdot10^{-2}$ mol/m^3 in the “loose” regions, while the “large” geometry (b) exhibits maxima of C-C_b of ~$1.6\cdot10^{-1}$ mol/m^3 in the “dense” regions and minima of ~$4\cdot10^{-2}$ mol/m^3 in the “loose” regions, with a range ~4 times wider than the “small” one.

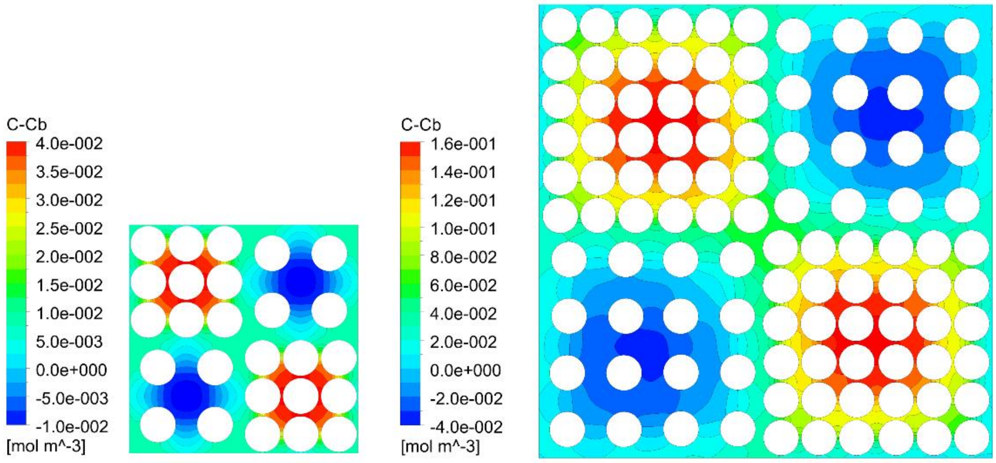

(a) (b)

Figure 17: False color maps of the difference between local and bulk concentration over a cross section of the computational domain for the (a) “small” and (b) “large” geometries at Sc=1.

Axial profiles of the “dense” and “loose” bulk concentrations for Sc=500 are reported in **Figure 18**. As remarked above, for this value of Sc, a very long computational domain, ~36,000d in extent, was adopted since the concentration development length is proportionally larger. The price of some loss of accuracy was paid since the number of finite volumes along the flow direction z was kept fixed at 110 as in the case Sc=1 in order to limit the computational effort.

As in the previous case Sc=1, larger length scales yield larger differences between the bulk concentrations of “dense” and “loose” regions. The 1% development length $z_{dev,C}$ is much larger than in the Sc=1 case (~20,000d for both geometries), due to the larger Schmidt number. Note that the graphs in **Figure 16** and **Figure 18** exhibit the same general trend but are not in similarity; the reason is that, of the two terms at the right hand side of Eqs. (30) and (31), the first expresses the “adiabatic” increase in concentration due to scalar influx from the fibers and is independent of the Schmidt number, while the second expresses the scalar flux from “dense” to “loose” regions (which, in the hydrodynamically fully developed region, is purely diffusive) and thus depend on Sc.

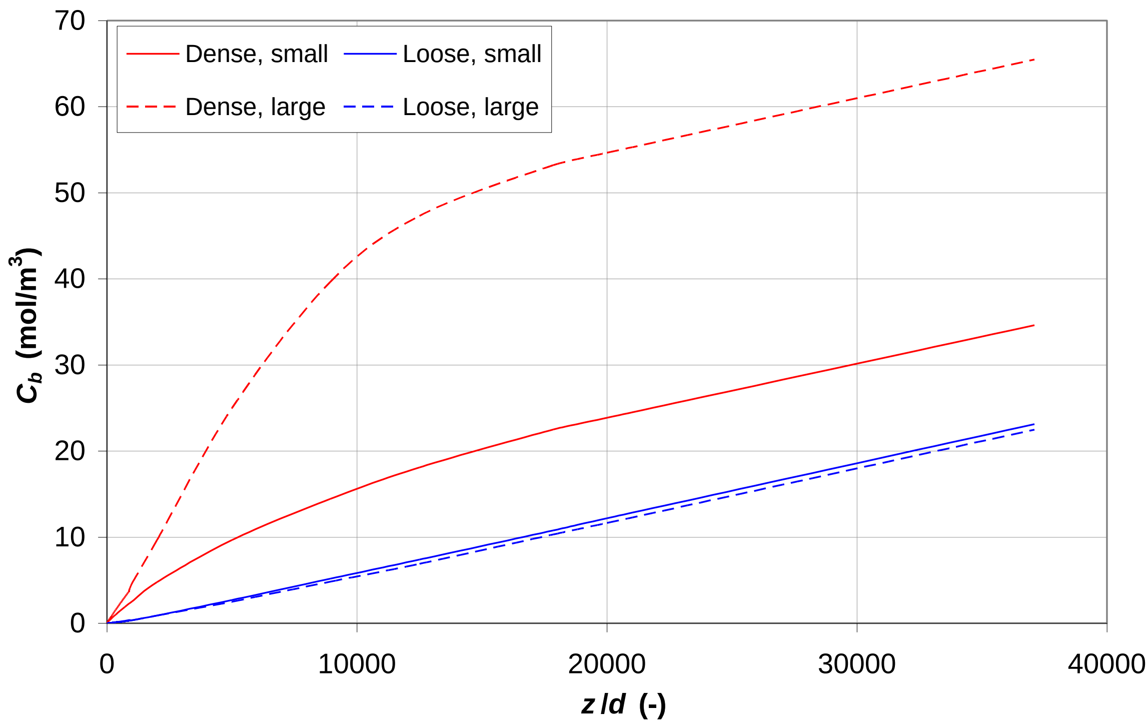

Figure 18: Bulk concentrations in the "dense" and the "loose" regions of the bundle as a function of the dimensionless axial coordinate z/d at Sc=500 for the two geometries simulated.

Concentration maps for this case are similar to those in **Figure 17** and are not reported here for brevity.

A second possible definition of the mass transfer development length, say, $z_{dev,\mathrm{Sh}}$, can be based on the behavior of the Sherwood number. For example, **Figure 19** reports Sherwood numbers as functions of the dimensionless axial coordinate z/d for Re=10 and Sc=1.

In particular, **Figure 19**(a) shows the separate values of Sh in the "dense" (ε=0.31) and "loose" (ε=0.69) regions in the "large" (4×4&6×6) geometry along with the corresponding mean Sh. The dashed line represents the Sherwood number for an infinite regular square array at the same Sc and the same mean porosity ε=0.5. A first striking feature of this graph is that the Sherwood number is much lower than that predicted for a regular fiber array in both the "dense" and the "loose" regions. A second noteworthy feature is that the mean Sh is lower than those separately computed for both regions. A third, somewhat expected, characteristic of the plot is that fully developed Sh values are attained far downstream than in a regular array. In particular, $z_{dev,\mathrm{Sh}}$ (defined, for example, as the value of z at which the Sherwood number approaches its asymptotic value within 1%) is ~2-3·d for the regular array but ~100-200·d for the non-uniform geometry, with larger values in the "loose" regions. In terms of the dimensionless variable $z^*=z/(d\mathrm{Pe})=1/\mathrm{Gz}$ (Gz being the Graetz number), Sh attains its fully developed value to within 1% at $z^* \approx 0.10$-0.15 for the regular array and $z^* \approx 5$-10 for the non-uniform configuration.

Figure 19(b) compares axial profiles of the mean Sh for the "small" (2×2&3×3) and "large" (4×4&6×6) geometries. As in the previous graph, the dashed line represents the Sherwood number in an infinite square array at ε=0.5. The 1%-fully developed Sherwood number is attained at $z_{dev,\mathrm{Sh}} \approx 200d$ in the "large" geometry and $z_{dev,\mathrm{Sh}} \approx 100d$ in the "small" geometry, consistently with the values of the development length derived above from concentration profiles for this Schmidt number.

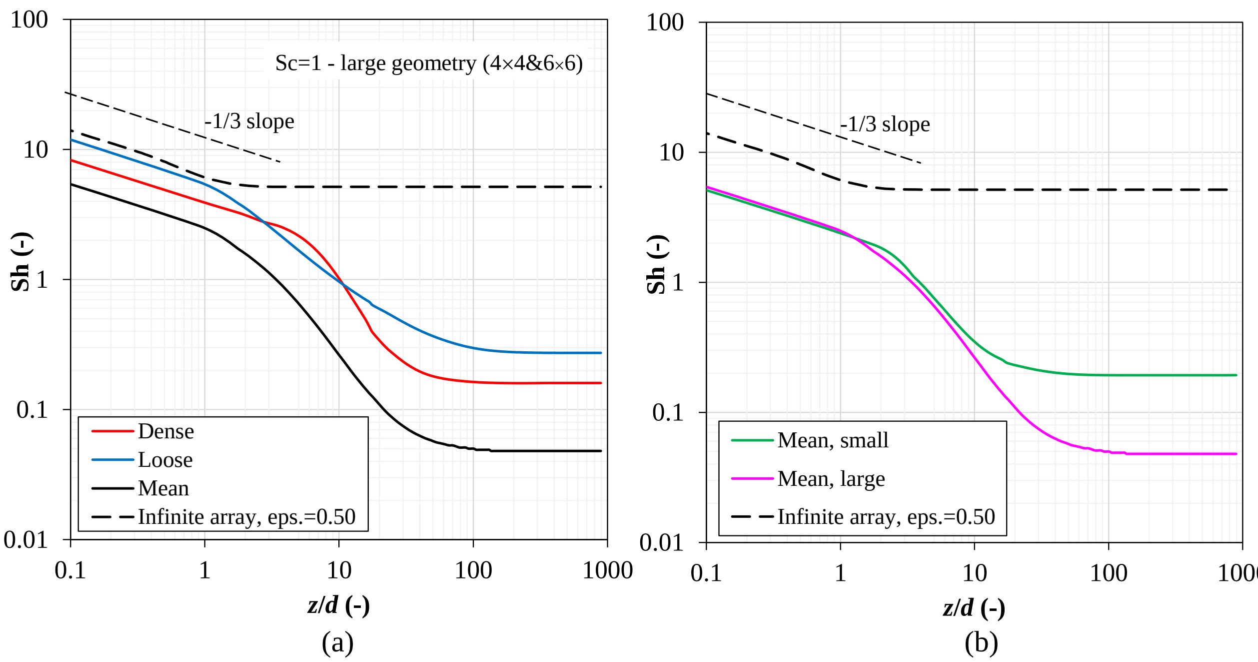

Figure 19: Sherwood numbers as functions of the dimensionless axial coordinate z/d for Re=10 and Sc = 1. (a) Separate Sh in the "dense" (ε=0.31) and "loose" (ε=0.69) regions and mean Sh for the "large" (4×4&6×6) geometry; (b) mean Sh for the "small" (2×2&3×3) and "large" (4×4&6×6) geometries. The dashed line reported in both graphs represents the Sherwood number for an infinite regular square array at the mean porosity ε=0.5.

Figure 20 reports Sherwood numbers as functions of the dimensionless axial coordinate z/d for Re=10 and Sc = 500. As in **Figure 19**, graph (a) shows the separate values of Sh in the "dense" (ε=0.31) and "loose" (ε=0.69) regions in the "large" (4×4&6×6) geometry along with the corresponding mean Sh, while graph (b) compares the mean Sh for the "small" (2×2&3×3) and "large" (4×4&6×6) geometries; the dashed line represents the Sherwood number for an infinite regular square array at the mean porosity ε=0.5 and the present Schmidt number of 500.

In comparison with the results for Sc=1 in **Figure 19**, the main difference is that all mass transfer development lengths are now ~200 times larger, i.e. between 20,000 and 40,000 (an increase lower than the 500-fold increase in the Schmidt number), so that the length of the computational domain (~36,000d) is barely sufficient to allow fully developed conditions to be achieved. Minor differences regard the shape of the Sh-z curves, which are now more complex than in the case Sc=1, probably due to the larger relative magnitude of advective scalar fluxes, associated with flow redistribution between regions at different porosity, with respect to diffusive scalar fluxes. Asymptotic Sh values, on the other hand, are the same as those predicted for Sc=1, consistently with the fact that in parallel flow the Sherwood number does not depend on the Schmidt number. As in the case Sc=1, the asymptotic overall, or mean, Sherwood number is smaller than either the "dense" or "loose" Sh, and decreases as the length scale of the non-uniformity increases.

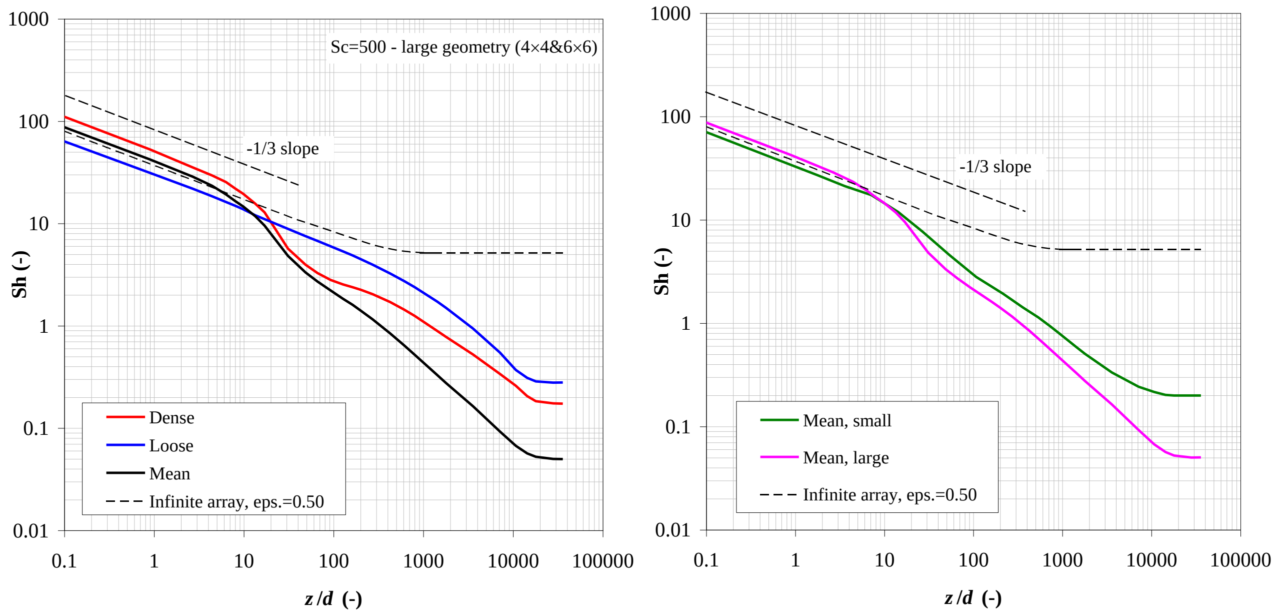

(a) (b)

Figure 20: Sherwood numbers as functions of the dimensionless axial coordinate z/d for Re=10 and Sc = 500. (a) Separate Sh in the "dense" (ε=0.31) and "loose" (ε=0.69) regions and mean Sh for the "large" (4×4&6×6) geometry; (b) mean Sh for the "small" (2×2&3×3) and "large" (4×4&6×6) geometries. The dashed line reported in both graphs represents the Sherwood number for an infinite regular square array at the mean porosity ε=0.5.

Conclusions

The effects of a non-uniform porosity distribution on low-Reynolds number hydrodynamics and mass transfer in a bundle of parallel fibers were investigated. To this purpose, a straight channel in axial flow, made up of regions filled with regular arrays of identical cylindrical fibers of two different porosities, was studied as the model system.

In a first stage, all interactions between "dense" and "loose" regions were neglected and fully developed flow and concentration fields were assumed. Consistently with the model's assumptions, previously obtained computational results for the Darcy permeability and the shell-side Sherwood number (based on the fiber diameter) in regular fiber arrays were assumed to hold in each region.

Elementary computations, repeated for different values of the mean porosity ε and of the ratio R of “loose” to “dense” porosity, showed that, within the non-uniform bundle, “loose” regions always exhibit, as expected, a larger Darcy permeability then “dense” regions. The behavior of the “loose” to “dense” Sherwood number ratio is more complex since its dependence upon the porosity in a regular fiber array is non-monotonic and exhibits a maximum at some intermediate porosity which, for square arrays and uniform wall mass flux conditions, is ~0.6.

More interesting is the behavior of overall Darcy permeability and Sherwood number, computed for the bundle as a whole: the non-uniformity causes in all cases a significant increase of the overall permeability and, almost in all cases, a very large decrease of the overall Sherwood number with respect to a uniform bundle of the same mean porosity, the only exception being the case of a slight non-uniformity (e.g., ratio of “loose” to “dense” porosities < 1.25) in conjunction with an unrealistically large mean porosity (e.g. >0.9). This behavior, although somewhat surprising, is consistent with previous findings by Lipscomb and co-workers (Bao and Lipscomb, 2002a) for random fiber arrays, exhibiting a similar non-uniformity in the distribution of the porosity. It can be intuitively explained by considering that most of the flow is diverted through the “loose” regions, characterized by few fibers, while very little fluid flows through the “dense” regions, where most fibers reside, causing poor overall mass transfer.

In a second stage, the model channel was assumed to be made of alternately “dense” and “loose” regions, disposed in a checkerboard arrangement and each filled with a regular array of fibers (for symmetry reasons, it was sufficient to consider a square cross section including only two “dense” and two “loose” sub-regions). Fully three-dimensional CFD simulations were conducted by assuming uniform velocity and concentration at the inlet (simultaneously developing flow and concentration fields). The simulated length of the channel was large enough for fully developed flow and mass transfer to be attained. Two different sizes of the “loose” and “dense” regions were considered, so that they included either 2×2 and 3×3 or 4×4 and 6×6 fibers, respectively. This approach allowed the effects of the hydrodynamic interaction and mass transfer between regions at different porosity to be assessed, also as a function of the length scale of the non-uniformity, and made the prediction of entry effects possible.

In regard to hydrodynamics, the simulations showed that the flow rate distribution between regions is somewhat intermediate between the uniform one expected in a regular array and the strongly non-uniform one predicted for non-interacting regions, the flow non-uniformity increasing (approaching that predicted for non-interacting regions) with the length scale of the geometrical non-uniformity. The hydrodynamic entry length is 2-3 times larger than that predicted for a uniform bundle (which is close to that expected in a circular pipe), but this increase seems to depend little on the geometrical length scale of the non-uniformity.

Also in regard to mass transfer, the CFD results for interacting regions and developing flow were consistent with those obtained for the hydrodynamic quantities, i.e. they were intermediate between those expected in a uniform bundle and those predicted by the simpler model assuming non-interacting regions and fully developed conditions. For "dense" and "loose" porosities of 0.69 and 0.31 (mean value ε=0.5, ratio R≈2.25,), the asymptotic (fully developed) overall Sherwood number was ~25 times smaller than in a uniform array at ε=0.5 for the smaller length scale (2×2 and 3×3 fibers), and ~100 times smaller for the larger one (4×4 and 6×6 fibers). This latter result is close to that obtained for non-interacting regions. The mass transfer development length was ~100 times larger than in a regular array (i.e., around a single fiber) for a Schmidt number of 1 and ~40 times larger for a Schmidt number of 500 (representative of many solutes in water). In this latter case, for a Reynolds number of 10 the mass transfer development length was of the order of $4 \cdot 10^4$ fiber diameters, thus largely exceeding the physical length of any realistic device employing hollow fibers. Also this large increase of the development length associated with bundle non-uniformity is consistent with the findings of Lipscomb and co-workers for random fiber arrays (Bao et al., 1999).

All the quantitative assessments in this paper were based on the assumption of square arrays of fibers. This configuration was chosen because it lends itself much more easily to build the "artificial", non-uniform, checkerboard geometry investigated in the second part of the study. However, the qualitative results and their order of magnitude are not expected to change significantly if more realistic hexagonal lattices or random fiber distributions are considered.

Similarly, through most of the paper the scalar transfer between the fibers and the working fluid is understood to be mass transfer, i.e. to regard a solute, and is described in terms of Schmidt and Sherwood numbers. However, the phenomenon studied can also be interpreted as a heat transfer problem, and the above numbers can be interpreted as Prandtl and Nusselt numbers, thus making the conclusions applicable (for example) to mini-heat exchangers and similar heat transfer devices.

Acknowledgments

Part of this work was carried out with the financial support of the *Programma Operativo Nazionale Ricerca e Innovazione 2014-2020 (CCI 2014IT16M2OP005), Fondo Sociale Europeo, Azione I.1 "Dottorati Innovativi con caratterizzazione Industriale"*.

Nomenclature

A	total cross sectional area of a porous channel (m^2)
C	concentration (mol m^{-3})
D	scalar diffusivity (m^2 s^{-1})
d	outer diameter of a fiber (m)
Gz	Graetz number based on fiber diameter, dPe/z (-)
j	mass flux at the wall (mol m^{-2} s^{-1})
K	axial Darcy permeability based on interstitial velocity (m^2)
L	length along x and y directions (m)
N	number of fibers (-)
n	number of fibers on each side (-)
P	pitch (center-center distance between adjacent fibers) (m)
p	pressure (Pa)
Pe	Péclet number, Re·Sc (-)
Q	flow rate (m^3 s^{-1})
R_ε	porosity ratio, $\varepsilon_l/\varepsilon_d$ (-)
Re	Reynolds number based on interstitial velocity and fiber diameter (-)
Sc	Schmidt number (-)
Sh	Sherwood number (-)
$\vec{u}$	local velocity (m s^{-1})
w	local velocity component along the axial direction z (m·s^{-1})
x, y	Cartesian coordinates in cross section orthogonal to the fibers (m)
z	Cartesian coordinate along the axial direction (m)
z^*	dimensionless axial coordinate, z/(dPe) (m)
$z_{dev,C}$	mass transfer development length based on concentration profiles (m)
$z_{dev,\mathrm{Sh}}$	mass transfer development length based on Sherwood number profiles (m)
$z_{h,dev}$	hydraulic development length (m)

Greek symbols

ε	generic or mean porosity (-)
μ	dynamic viscosity (Pa s)
ρ	density (kg m^{-3})

Subscripts

b	bulk (mass flow averaged)
c	critical
d	“dense” (low porosity)
$d \rightarrow l$	from “dense” to “loose” regions
l	“loose” (high-porosity)
min	minimum
r	region (i.e. “dense” or “loose”)
tot	total
$unif$	uniform
w	wall
ε	porosity
0	inlet section
∞	fully developed value

Averages

$\overline{\cdot}$	line average on fiber-fluid interface
$\langle \cdot \rangle$	surface average on fluid cross sectional area (interstitial mean value)

References

Ando, S., Nishikawa, M., Kaneda, M., Suga, K., 2022. Numerical simulation of filtration processes in the flow-induced deformation of fibrous porous media by a three-dimensional two-way fluid–structure interaction scheme. Chem. Eng. Sci. 252, 117500. https://doi.org/10.1016/j.ces.2022.117500.

ANSYS CFX Reference Guide Release 18.2, 2018.

Bao, L., Lipscomb, G.G., 2002a. Well-developed mass transfer in axial flows through randomly packed fiber bundles with constant wall flux. Chem. Eng. Sci. 57, 125–132. https://doi.org/10.1016/S0009-2509(01)00368-2

Bao, L., Lipscomb, G.G., 2002b. Mass transfer in axial flows through randomly packed fiber bundles with constant wall concentration. J. Memb. Sci. 204, 207–220. https://doi.org/10.1016/S0376-7388(02)00043-1

Bao, L., Liu, B., Lipscomb, G.G., 1999. Entry mass transfer in axial flows through randomly packed fiber bundles. AIChE J. 45 (11), 2346–2356. https://doi.org/10.1016/S0927-5193(03)80004-9

Cancilla, N., Gurreri, L., La Rosa, M., Ciofalo, M., Cipollina, A., Tamburini, A., Micale, G., 2023. Influence of bundle porosity on shell-side hydrodynamics and mass transfer in regular fiber arrays: A computational study. Int. J. Heat Mass Transf. 203, 123841. https://doi.org/https://doi.org/10.1016/j.ijheatmasstransfer.2022.123841

Cancilla, N., Gurreri, L., Marotta, G., Ciofalo, M., Cipollina, A., Tamburini, A., Micale, G., 2022.

Performance Comparison of Alternative Hollow-Fiber Modules for Hemodialysis by Means of a CFD-Based Model. Membranes (Basel). 12, 118. https://doi.org/10.3390/membranes12020118

Cancilla, N., Gurreri, L., Marotta, G., Ciofalo, M., Cipollina, A., Tamburini, A., Micale, G., 2021. CFD prediction of shell-side flow and mass transfer in regular fiber arrays. Int. J. Heat Mass Transf. 168, 120855. https://doi.org/https://doi.org/10.1016/j.ijheatmasstransfer.2020.120855

Ding, W., He, L., Zhao, G., Luo, X., Zhou, M., Gao, D., 2004. Effect of Distribution Tabs on Mass Transfer of Artificial Kidney. AIChE J. 50, 786–790. https://doi.org/https://doi.org/10.1002/aic.10073

Everts, M., Meyer, J.P., 2020. Laminar hydrodynamic and thermal entrance lengths for simultaneously hydrodynamically and thermally developing forced and mixed convective flows in horizontal tubes. Exp. Therm. Fluid Sci. 118, 110153. https://doi.org/10.1016/j.expthermflusci.2020.110153

Frank, A., Lipscomb, G.G., Dennis, M., 2001. Visualizing the entrapment of air pockets in the shell of a hemodialyzer during wet-out. Chem. Eng. Commun. 184, 139–155. https://doi.org/10.1080/00986440108912845

Frank, A., Lipscomb, G.G., Dennis, M., 2000. Visualization of concentration fields in hemodialyzers by computed tomography. J. Memb. Sci. 175, 239–251. https://doi.org/https://doi.org/10.1016/S0376-7388(00)00421-X

Happel, J., 1959. Viscous flow relative to arrays of cylinders. AIChE J. 5, 174–177. https://doi.org/10.1002/aic.690050211

Ishimi, K., Koroyasu, S., Hikita, H., 1987. Mass transfer in creeping flow past periodic arrays of cylinders. J. Chem. Eng. Japan 20(5), 492–498.

Kim, J.C., Cruz, D., Garzotto, F., Kaushik, M., Teixeria, C., Baldwin, M., Baldwin, I., Nalesso, F., Kim, J.H., Kang, E., Kim, H.C., Ronco, C., 2013. Effects of dialysate flow configurations in continuous renal replacement therapy on solute removal: Computational modeling. Blood Purif. 35, 106–111. https://doi.org/10.1159/000346093

Kim, J.C., Kim, J.H., Sung, J., Kim, Hyo Cheol, Kang, E., Lee, S.H., Kim, J.K., Kim, Hee Chan, Min, B.G., Ronco, C., 2009. Effects of arterial port design on blood flow distribution in hemodialyzers. Blood Purif. 28, 260–267. https://doi.org/10.1159/000232934

Łabęcki, M., Piret, J.M., Bowen, B.D., 1995. Two-dimensional analysis of fluid flow in hollow-fibre modules. Chem. Eng. Sci. 50, 3369–3384. https://doi.org/10.1016/0009-2509(95)00185-8

Lemanski, J., Lipscomb, G.G., 2002. Effect of shell-side flows on the performance of hollow-fiber gas separation modules. J. Memb. Sci. 195, 215–228. https://doi.org/https://doi.org/10.1016/S0376-7388(01)00561-0

Lemanski, J., Lipscomb, G.G., 2000. Effect of fiber variation on the performance of countercurrent hollow fiber gas separation modules. J. Memb. Sci. 167, 241–252. https://doi.org/10.1016/S0376-7388(99)00295-1

Lemanski, J., Lipscomb, G.G., 1995. Effect of shell-side flows on hollow-fiber membrane device performance. AIChE J. 41, 2322–2326. https://doi.org/https://doi.org/10.1002/aic.690411017

Lipscomb, G., Sonalkar, S., 2004. Sources of non-ideal flow distribution and their effect on the performance of hollow fiber gas separation modules. Sep. Purif. Rev. 33, 41–76. https://doi.org/10.1081/SPM-120030236

Liu, B., Lipscomb, G.G., Jensvold, J., 2001. Effect of fiber variation on staged membrane gas separation module performance. AIChE J. 47, 2206–2219.

https://doi.org/10.1002/aic.690471008

Miyagi, T., 1958. Viscous Flow at Low Reynolds Numbers past an Infinite Row of Equal Circular Cylinders. J. Phys. Soc. Japan. https://doi.org/10.1143/JPSJ.13.493

Noda, I., Brown-West, D.G., Gryte, C.C., 1979. Effect of flow maldistribution on hollow fiber dialysis - experimental studies. J. Memb. Sci. 5, 209–225. https://doi.org/10.1016/S0376-7388(00)80449-4

Noda, I., Gryte, C.C., 1979. Mass Transfer in Regular Arrays of Hollow Fibers in Countercurrent Dialysis. AIChE J. 25, 113–122.

Park, J.K., Chang, H.N., 1986. Flow distribution in the fiber lumen side of a hollow-fiber module. AIChE J. 32, 1937–1947. https://doi.org/10.1002/aic.690321202

Sangani, A.S., Yao, C., 1988. Transport processes in random arrays of cylinders. II. Viscous flow. Phys. Fluids 31, 2435–2444. https://doi.org/10.1063/1.866596

Sparrow, E.M., Loeffler, A.L., 1959. Longitudinal laminar flow between cylinders arranged in regular array. AIChE J. 5, 325–330. https://doi.org/10.1002/aic.690050315

Sun, L., Panagakos, G., Lipscomb, G., 2022. Effect of Packing Nonuniformity at the Fiber Bundle–Case Interface on Performance of Hollow Fiber Membrane Gas Separation Modules. Membranes (Basel). 12, 1139. https://doi.org/10.3390/membranes12111139

Wang, Yujun, Chen, F., Wang, Yan, Luo, G., Dai, Y., 2003. Effect of random packing on shell-side flow and mass transfer in hollow fiber module described by normal distribution function. J. Memb. Sci. 216, 81–93. https://doi.org/10.1016/S0376-7388(03)00048-6